


Original Research Article

Altered Electroencephalography Spectral Profiles in Rats with Different Patterns of Experimental Brain Dysplasia

Michał Kielbinski ^{1‡}, Zuzanna Setkowicz ^{1‡}, Kinga Gzielo¹, Władysław Węglarz², and Krzysztof Janeczko¹

BACKGROUND: Malformations of cortical development, such as focal cortical dysplasia, are commonly associated with intractable epilepsy. Multiple animal models were created in attempts to recapitulate features of human malformations of cortical development. These manipulations give rise to various focal or diffuse anatomical abnormalities, accompanied by altered susceptibility to epileptic seizures. Both in humans and in models of dysplasia, the question of timing of the initiating insult is important. **METHODS:** Here, we used a rat model of cerebral dysplasia elicited by prenatal irradiation at gestational days (E) 13, 15, 17, or 19. Previous results suggest these animals are characterized by different patterns of dysplasia as well as different reactivity to seizurogenic stimuli in several seizure models. Rats were implanted with telemetric electroencephalography (EEG) transmitters. We compared EEG data from freely moving animals with anatomical observations obtained with MRI, as well as Western blotting and immunohistochemistry. **RESULTS:** We

performed spectral analyses of EEG signal, revealing differential regulation of specific bands (including delta, theta, alpha-beta, gamma) in animals with different patterns of dysplasia. Relative contribution of low-frequency activity in delta band is the lowest in E15 and the highest in E19. Conversely, higher frequency bands, corresponding to alpha/beta and gamma components, are reduced in E15 versus E19. This is accompanied by altered expression of glial markers in the E19 group. **CONCLUSION:** To our knowledge, this constitutes the first quantitative description of power spectral properties in this experimental model, providing insight into mechanisms underlying the anatomical and electrophysiological abnormalities associated with brain dysplasia of different types. Birth Defects Research 00:000–000, 2017. © 2017 Wiley Periodicals, Inc.

Key words: neurogenesis; gamma irradiation; brain dysplasia; epilepsy; EEG; MRI

INTRODUCTION

Focal cortical dysplasia (FCD) is a commonly associated with intractable epilepsy. In children and adolescents undergoing epilepsy surgery, FCD is the most common etiology (Harvey et al., 2008; Lerner et al., 2009). The currently used classification comprises three main types, with several subtypes (Blümcke et al., 2011; Ochoa et al., 2017) distinguished by major anatomical and histological features. The etiology of brain malformations is generally linked to disturbed prenatal or early postnatal development, in particular, impaired neurogenesis or neuronal migration (Barkovich et al., 2012). The molecular and cellular mechanisms leading to the development of malformations of cortical development (MCD) are studied with different animal models addressing distinct subtypes or aspects of FCD (Luhmann, 2015; Wong and Roper, 2016).

Despite these developments, there is still an ongoing need for refinement (Pitkänen et al., 2016).

An area especially open for improvement is the modeling of type I FCD and similar pathologies, like the “mild” dysplasia. Here, pre- and perinatal insults, perhaps combined with specific genetic background, are often proposed as potential causative factors (Marín-Padilla et al., 2002; Widdess-Walsh et al., 2005; Krsek et al., 2010). Prenatal gamma irradiation in rats—where a developmental insult generates dysplasia with impaired cortical cytoarchitecture and lamination, thinned cortical mantle and several additional pathologies, such as dispersion of hippocampal neurons and subcortical heterotopias—has been proposed as a potentially useful experimental model similar to FCD type I (Luhmann, 2015; Roper, 1998; Roper et al., 1995; Wong and Roper, 2016).

Some features critical to this model have been well described, such as altered susceptibility to seizurogenic agents (usually in the absence of behavioral spontaneous seizures) and hyperexcitability (Roper, 1998; Kondo et al., 2001; Kellinghaus et al., 2004). There is also evidence of impaired performance in behavioral tasks, especially those involving hippocampal memory, like place and object recognition (Zhou et al., 2011; Zhou and Roper, 2012). In general, proposed mechanisms involve shifted excitation-inhibition balance, due to loss of gamma-aminobutyric acid (GABA)ergic signaling by means of decreased interneuron number, efficacy and connectivity (Roper et al., 1999; Zhu and Roper, 2000; Zhou and Roper, 2011, 2014)

¹Department of Neuroanatomy, Institute of Zoology, Jagiellonian University, Krakow, Poland

²Department of Magnetic Resonance Imaging, Institute of Nuclear Physics, Polish Academy of Sciences, Krakow, Poland

Supported by the Polish National Science Centre grant 2011/01/B/NZ4/00586.

[‡]These authors contributed equally to this work.

Conflicts of Interest: The authors declare no conflicts of interest.

*Correspondence to: Michał Kielbinski, Institute of Zoology, Jagiellonian University, Gronostajowa 9, 30-387 Krakow, Poland. E-mail: michal.kielbinski@uj.edu

Published online 0 Month 2017 in Wiley Online Library (wileyonlinelibrary.com).
DOI: 10.1002/bdr2.1131

with concomitant enhancement of glutamatergic transmission (Chen et al., 2007).

It is proposed that the loss of migrating neuroblasts and radial glial cells underlies the generation of dysplasia in this model (Wong and Roper, 2016). What follows from this assumption, is the anticipation of different time points of irradiation giving rise to distinct “patterns” of dysplasia. This has been a major focus of our previous studies, where we reported different susceptibility of animals with dysplasia induced on different days of gestation (E13, E15, E17, or E19) to seizurogenic stimuli: pilocarpine, kainic acid, or electric stimulation (Setkowicz et al., 2003, 2005, 2014). Notably, while pilocarpine seizure susceptibility was increased in animals irradiated late, that is, at E17 and E19 but not E13 and E15, the vulnerability to kainate followed an opposite trend (higher in the earlier groups). In the electric shock model, the expression of two types of seizure activity (tonic vs. clonic) was also differentially affected. Thus, our first goal in the present study was to provide an extended anatomical description of these patterns of dysplasia and their relation to function.

Prior electroencephalography (EEG) research in the prenatal irradiation model has been mostly focused on spontaneous “interictal” spikes, rather than the general description of activity in the dysplastic cortex. In light of the behavioral deficits in these animals and the often observed clinical correlation between epilepsy and mental or behavioral comorbidities (Gulati et al., 2014), a more general description of the state of dysplastic brain activity could be potentially useful. Thus, we asked whether gross patterns of EEG activity are affected by dysplasia even in the absence of seizures.

Finally, while the immediate disruption of migration and maturation of neuronal precursors is a natural target in this model, there is evidence of long-term maladaptive changes in the brain, such as altered expression of genes related to plasticity and cell survival (Hiremath et al., 2009). Here, we ask about potential changes in hippocampal astrocytes, which were previously only briefly explored in this model (Janeczko et al., 1999), despite mounting evidence of glial involvement in the pathogenesis of brain malformations (Sosunov et al., 2008; Talos et al., 2008; Kielbinski et al., 2016). Astrocytes in rats are generated postnatally and their functional maturation happens over several weeks (Bushong et al., 2004), but molecular events that underlie gliogenesis have been found during gestation (Miller and Gauthier, 2007). We hypothesized that these processes would indeed be affected, especially in the late irradiated E19 group.

Here, we used MRI of adult rat brains with cerebral dysplasia induced at E13, E15, E17, or E19 to determine the frequency and severity of features such as heterotopias; as well as estimate brain and hippocampal volume. This was accompanied by analyses of EEG spectral composition. In addition, we performed immunoblotting assays

for several glial markers (glial fibrillary acidic protein [GFAP], glutamine synthetase (GS), connexin 43, inwardly rectifying potassium channel Kir4.1 and glutamate receptor subunit Glur4) as well as immunohistochemical staining for GFAP. Together, these data could be useful in answering further questions, such as: what differentiates the various patterns of dysplasia? How do the effects of irradiation at other time points relate to the (most commonly studied) E17? Does altered brain anatomy correlate with patterns of EEG activity? Can underlying changes in astrocytes in the dysplastic brain be detected even in the absence of seizures?

MATERIALS AND METHODS

ETHICAL CONCERNS

All experimental procedures were compliant with the European Communities Council Directive (2010/63/EU) and were approved by the Animal Care and Use Committee of the Jagiellonian University (decision no. 122/2011). All efforts were made to minimize animal suffering, as well as to minimize the number of animals used in the experiment.

ANIMALS

Experimental gamma irradiation was performed as described previously (Setkowicz et al., 2014). Briefly, pregnant female Wistar rats were whole-body irradiated from a ^{60}Co gamma ray source (Institute of Nuclear Research, Polish Academy of Sciences, Krakow), with a total dose of 1 Gy per animal. Each female was irradiated on a specific day of gestation, randomly assigned. The days were E13, E15, E17, or E19. Untreated (N, naïve) females provided experimental controls.

Male offspring of these dams constituted the actual experimental animals. At 21 days of age, these rats were weaned off and maintained under conditions of controlled temperature ($20 \pm 2^\circ\text{C}$) and a 12/12 hr light/dark cycle. Standard laboratory feed (Labofeed) and water were available ad libitum. At 55 days, the experimental animals underwent surgical implantation of telemetric EEG devices.

The total number of animals used in the main experiment was, as follows: E13 $n = 18$, E15 $n = 20$, E17 $n = 20$, E19 $n = 21$, and N rats, $n = 18$. Group numbers were constrained by the ability to obtain them (i.e., litter sizes and sperm-positive females giving birth), and the ability to obtain good quality EEG or MRI data. The number of animals per group for each experimental method is given in their respective sections in the Materials and Methods.

In addition, age-matched animals from corresponding groups (E13–E19 and naïve controls, $n = 6$ per group) were used for immunoblotting. These rats did not undergo transmitter implantation.

TELEMETRIC EEG ACQUISITION

Animals were anesthetized with 2 to 4% inhaled isoflurane (Aerrane, Baxter) in oxygen. An incision was made in the skin on the side and a portable rodent telemetry transmitter (TA11CTA-F40 Implant, Data Sciences International) was inserted under the skin. Two biopotential leads (positive and reference) were guided toward the animal's head subcutaneously. Two holes were drilled in the skull: one parietal, halfway between the Bregma and Lambda points, one occipital above the cerebellum, for the positive and reference lead, respectively. The leads were placed on the exposed dura, held in place with dental cement (Duracryl Plus, Spofa Dental), and the skin above the cement cap was sutured. The surgeries were carried out in aseptic conditions, and animals were given proper post-op care. Antibiotics (Sul-Tridin, Norbrook Laboratories Ltd) and nonsteroid anti-inflammatory drugs (Tolfedine, Vetaquinol SA) were administered.

After surgery, rats were placed in single cages and given 2 weeks to heal before any further experimental procedures were carried out. Beginning 2 weeks after surgery (postnatal day 70), electroencephalographic data was recorded continuously at 500 Hz sampling rate from all animals using DSI receiver plates and DSI Acquisition software. For all animals, 48 hr of continuous data (all starting around 9 a.m.) was acquired.

EEG SIGNAL ANALYSIS

Raw EEG data were transferred into the Spike2 program, which was subsequently used for further analysis. Based on initial inspection of the waveforms, an amplitude window was selected and all activity crossing the threshold was marked in a separate event channel. This was followed by a second round of visual inspection, during which any additional artifacts missed by the initial procedure were marked. Our initial observations suggest that the main sources of artifacts were: animal motion (such as chewing, scratching) and momentary loss of wireless signal, resulting in sharp, very high-power spikes with extreme amplitude. All signal in 10-sec time windows from any marked artifact was excluded from further analysis. We also identified animals in which, likely due to mechanical damage to the insulation of the biopotential leads, or to contamination of the signal with electrocardiographic noise, this approach was unsuccessful. These recordings were excluded completely.

The resulting signal was processed with fast Fourier transform with a Hanning window of width = 256, corresponding to 128 bins of width = 1.953 Hz and epochs of 0.5 second. Frequencies from approximately 2 to 67 Hz were used for further analysis.

Principal component analysis (PCA) was performed in the frequency domains with relative spectral densities over the entire sampling period (32 total input variables, each corresponding to a single bin obtained from fast

Fourier transform). The rationale was that adjacent frequencies that vary together form EEG bands. The first two components obtained from PCA contained 89.2% of the cumulative variance: 72% for the first and 17.2% for the second component, respectively. Component loadings were then examined: concurrent variables (corresponding to adjacent EEG bins) with similar loadings for the first two components were grouped together. Similarity was defined as loadings having the same sign (positive or negative, with values above 0.1) or near-zero (value < 0.1).

As a result, we have constructed empirical bands which corresponded to physiological bands (alpha, beta, gamma, delta, and theta). The bands analyzed are as follows: "delta" (approximately 2–6 Hz), "theta" (approximately 6–10 Hz), "alpha/beta" (approximately 10–32 Hz). The highest frequency band (approximately 32–67 Hz) was analyzed as two separate sub-bands "gamma 1" (approximately 32–45 Hz) and "gamma 2" (approximately 45–67 Hz).

We then normalized the signal in each band to the sum of all bands. This relative power metric was taken as a measure of the contribution of the specific band to the overall activity.

In total, 64 total animals were used for EEG power analysis: E13, $n = 12$; E15, $n = 12$; E17, $n = 15$; E19, $n = 17$; and controls, $n = 9$.

SACRIFICE AND TISSUE PROCESSING

After the end of EEG acquisition phase, animals were given a lethal dose of sodium pentobarbital (Morbital, Biowet Pulawy) by means of intraperitoneal injection. Subsequently, they were perfused transcardially with 0.9% NaCl followed by 4% formalin (Chempur) in phosphate buffer (pH 7.4). Brains were removed, postfixed in the same formalin solution used for perfusion fixation, then cut into 30- μ m coronal sections on a Vibratome (VT 1000S, Leica).

Rats used for immunoblotting were sacrificed by decapitation, brains were removed, followed by bilateral excision of hippocampi, which were then placed in pre-cooled single plastic tubes and stored for later use.

EX VIVO MRI

Imaging was performed at Department of Magnetic Resonance Imaging, Institute of Nuclear Physics, Polish Academy of Sciences, Krakow, Poland. T2-weighted scans of formalin-fixed rat brains were obtained with a Bruker Biospec 94/20 device with a horizontal superconducting 9.4 Tesla magnet (rapid spin echo sequence was used, pulse characteristics: repetition time 2000 ms, echo time 42.94 ms, echo train length = 16; flip angle: 180°) at a final XY resolution of 0.025 mm per pixel and Z depth of 0.1 mm within a 25.6 mm² field of view. Scans were performed with Bruker ParaVision 5.1 software, then aligned to a coronal view and exported as .tiff image stacks for use with ImageJ.

For volume estimation of whole brains and hippocampal formations, the Volumest plugin was used (<http://lepo>).

TABLE 1. Descriptive statistics of experimental groups used in the study.

Group	Total <i>N</i> (MRI)	Normal	Mild heterotopia	Intermediate heterotopia	Severe heterotopia
E13	17	8 (47%)	1 (6%)	3 (18%)	5 (29%)
E15	19	9 (47%)	2 (11%)	4 (21%)	4 (21%)
E17	20	0	16 (80%)	3 (15%)	1 (5%)
E19	16	13 (81%)	2 (13%)	1 (6%)	0
N	18	18 (100%)	0	0	0

it.da.ut.ee/~markkom/volumest). This is a semi-automated implementation of the Cavalieri stereological method, where randomly aligned square grids of constant cell size are overlaid on optical slices containing the structure of interest, which is then outlined manually by the investigator. Crossing points between the measuring grid and the outlined structure of interest are counted and used for estimating the surface area on each slice. Because the alignment of the grid on each axial section is randomized, this results in unbiased estimation of surface area for each axial slice (estimated from the number of intersections between the grid and the structure) from which, subsequently, a volume estimate \hat{V} is obtained given the known distance between slices (Roberts et al., 2000). For an object of volume V , transected by i planes (optical slices) of depth z , on which P_i intersection points were found with a grid with cell size $\hat{V} = u^2 z^* \sum P_i$.

Using this method, we obtained total brain volumes, from rostral olfactory cortex to the end of the cerebellum (grid size $u = 1.4$ mm; slice depth $z = 0.4$ mm) and the hippocampal volumes, from the frontal part to the level of lateral geniculate, where the border between the hippocampus and overlying cortex becomes blurred in T2 images ($u = 0.2$ mm; $z = 0.4$ mm).

The total number of animals used for volume estimation per group was: $n = 6$ for E13; $n = 10$ for E15; $n = 11$ for E17; $n = 8$ for E19; and 14 controls. For classification of gross anatomical features, we also included additional image series, for a total of 16 to 20 representative image series per experimental group (see Table 1).

IMMUNOBLOTTING

Frozen hippocampi were thawed, fragmented mechanically, and homogenized with a handheld rotor-stator device (Omni Tissue Homogenizer, Omni International) in $4 \times$ volume of homogenization buffer (50 mM Tris-HCl, 100 mM NaCl, 0.5% sodium deoxycholate, 0.5% NP-40, 0.5% sodium dodecyl sulphate, pH = 7.5), then centrifuged for 15 min at 4°C. Supernatant was collected and protein concentration was measured spectrophotometrically (DS-11, DeNovix Inc.). Aliquots of these extracts were diluted to the concentration of 40 µg/µl. They were then diluted 1:1 (v:v) in loading buffer (125 mM Tris-HCl, 4% sodium

dodecyl sulphate, 25% glycerol, 4 mM ethylenediamine tetraacetic acid, 20 mM dithiothreitol, 0.01% bromophenol blue, pH = 6.8) and denatured for 4 min in 96°C. All reagents were obtained from Sigma Aldrich, unless noted otherwise.

Polyacrylamide gel electrophoresis was performed in ready-made 4 to 20% gradient gels (MiniProtein TGX Stain Free, Bio-Rad) under constant voltage (60 V) for 30 min followed by 150 V for 60 min. Wet transfer was performed for 60 min (constant 350 mA current, starting voltage 100 V), onto 0.45 µm pore size polyvinylidene fluoride membranes (Millipore). Membranes were briefly rinsed in Tris-HCl buffer (TBS), the stain-free signal visualized briefly (GelDoc tabletop imager, Bio-Rad). Subsequently, the membranes were transferred for 60 min into TBS with 0.1% Tween20 (TBS-T) with 5% fat-free milk for blocking. This was followed by incubation with primary antibodies in TBS-T in 5% milk overnight at 4°C. The primary antibodies used were: polyclonal rabbit anti-GFAP (1:2000; DAKO Z0334), polyclonal rabbit anti-connexin 43 (Cx43; 1:2000, Sigma C-6219), polyclonal rabbit anti-inward-rectifying potassium channel Kir4.1 (1:1000, Alomone Labs APC-035), monoclonal rabbit anti-AMPA receptor Glur4 (1:1000, Cell Signaling 8070P), monoclonal mouse anti-GS (1:2000, Chemikon MAB302).

Membranes were then collected, washed extensively in TBS and incubated with secondary antibodies conjugated with horseradish peroxidase (goat anti-rabbit or goat anti-mouse, 1:10,000, Cell Signaling), rinsed again, then Western blotting signal was visualized using the chemiluminescent Clarity reagent (Bio-Rad) with a ChemiDoc scanner (Bio-Rad). Protein-specific signal was taken as a semi-quantitative measure of the amount of protein of interest on the membrane, while the initial “stain-free” signal (an in-gel covalently binding protein marker) was used as a similar measure of total protein abundance. Western signal was then normalized to the total protein signal for each sample, and each sample was standardized using the sum of normalized sample signal within each set of replicates, corresponding to all experimental groups (Degaspero et al., 2014). For each protein of interest and each experimental group, six biological replicates (animals) were used.

IMMUNOHISTOCHEMICAL STAINING

For immunostaining, free-floating slices were incubated overnight with primary antibody against GFAP (DAKO Z0334, 1:2000) in TBS (0.05 M Tris [Sigma T-1378] and 0.9% NaCl, pH 7.6). Immunopositive cells were visualized using the avidin-biotin reaction (Vectastain ABC kit, Vector).

Immunostained brain sections were photographed under a light microscope using a digital camera (Nikon Microphot SA). Multiple images were collected under a 10x objective and stitched together with Microsoft ICE to form panoramic images spanning the entire hippocampal formation (see Fig. 4A). Each panorama consisted of 35 to 45 single frames representing the entire structure at Bregma -3.30 to -3.60 , according to Paxinos and Watson (Paxinos and Watson, 1998).

Immunoreactive area measurements were performed on the panoramic images by first thresholding using a semi-automatic, unsupervised local contrast enhancement and thresholding algorithms. Briefly, the images were split into their component channels and the G channel was selected, locally contrast enhanced using the ImageJ implementation of contrast limited adaptive histogram equalization, followed by local thresholding with the Bernsen algorithm (filter radius: 115 pixels. The binary images were size-filtered with a high-pass filter (Analyze Particles ImageJ function, area threshold = 999 pixels) to remove debris and point noise (Fig. 4B). All parameters were empirically selected on representative images from the experiment, then applied to all images by means of an ImageJ macro to reduce observer bias. Finally, the thresholded area was measured and the ratio between immunoreactive area and total hippocampal area ("Area Fraction") was used as a semi-quantitative measure of immunoreactivity. Animal number per group was: E13, $n = 16$; E15, $n = 10$; E17, $n = 14$; E19, $n = 12$, and 14 controls.

STATISTICAL ANALYSIS

Normality and homoscedasticity assumptions were checked by visual inspection of boxplots and Levene's F ratio testing. Parametric or nonparametric tests were then chosen based on deviation from normality. For consistency, all box plots in the figures illustrate the full span of all data points (whiskers), 25 to 75% quartiles (boxes) and median.

For EEG, the group effect was tested using one-way Kruskal-Wallis nonparametric tests with between-group comparisons done posthoc with median tests. For volumetric MRI and immunoblotting, one-way analysis of variance (ANOVA) was used; posthoc testing was performed with Tukey's honest significant difference (HSD) with appropriate corrections for unbalanced group N. Anatomical phenotype frequencies between groups were compared with Pearson's χ^2 and additional comparisons between animals with and without heterotopias were performed with Student's t test.

Relationships between estimated brain and hippocampal volumes and EEG composition were explored by fitting linear models for the effect of group (E13–E19, N), both anatomic variables and their interaction on the ratio between high and low band activity ($\alpha + \beta + \gamma_1 + \gamma_2 / \delta$). This ratio metric exhibited no significant deviation from normality assumptions, and was thus processed with ANOVA and Tukey's HSD.

For linear model fitting, estimated brain and hippocampal volumes were quantile normalized and expressed as z-scores (mean divided by standard deviation) to facilitate interpretation and allow easier comparisons between models. Estimates of coefficients were tested with single-sample t test to identify significant differences from zero. The goodness of fit of linear models was compared using the Akaike Information Criterion (AIC).

Most statistical analyses were performed in Statistica 10 (Statsoft), with the exception of exploratory PCA used for informing the choice of EEG bands and model fitting and comparisons, which were performed in R.

RESULTS

EEG COMPOSITION

Significant between-group differences in relative power (power in a band divided by total power in the studied frequencies 2–67 Hz) were detected in the delta band: Kruskal-Wallis $H(4,65) = 21.695$; $p = 0.0002$. Multiple comparisons by means of median tests revealed significant reductions in fractional delta power in E15 (mean rank = 16.5) when compared with E19 (mean rank = 43.5) and controls (mean rank = 44.8), respectively; as well as in E17 (mean rank = 24.1) compared with E19s (Fig. 1A).

The relative power in cumulated alpha and beta bands was also significantly different between groups, $H(4,65) = 29.435$; $p < 0.0001$. Median testing revealed an increase in this band in E15 (mean rank = 51.6) compared with E19 (mean rank = 23.2; $p = 0.0007$) and controls (mean rank = 13.4; $p < 0.0001$) as well as E17 (mean rank = 42.2) compared with E19 ($p = 0.05$) and controls ($p = 0.003$; Fig. 1C).

Similar direction of changes was observed in the gamma 1 band: $H(4, 65) = 18.019$, $p = 0.001$, which corresponded to a significant increase in E15 (mean rank = 49.9) versus E19 (mean rank = 21.9; $p = 0.0008$) and controls (mean rank = 25.8; $p = 0.04$; Fig. 1D), as well as the gamma 2 band: $H(4, 65) = 15.643$; significant increase in E15 (mean rank = 48.3) versus E19 only (mean rank = 20.5; $p = 0.001$; Fig. 1E).

No differences were found in theta activity: $H(4,65) = 5.671$, $p = 0.23$ (Fig. 1B).

To facilitate further exploration of the relationship between EEG power composition and anatomical features from MRI, an additional metric was constructed: the ratio

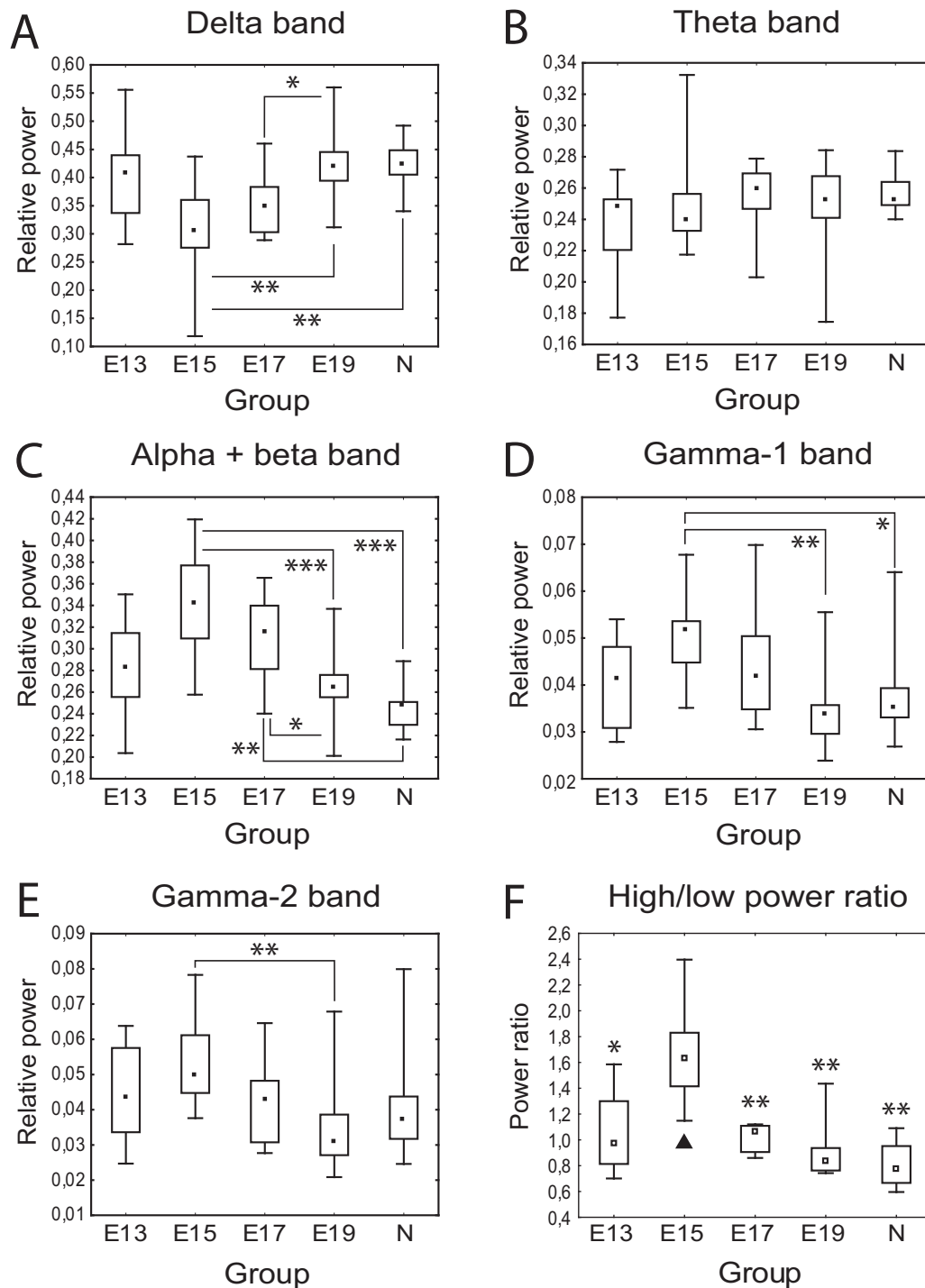


FIGURE 1. Relative EEG power (power in band/sum of power in all bands). (A) Delta band, 2–6 Hz. (B) Theta band, 6–10 Hz. (C) Combined alpha and beta bands, 10–32 Hz. (D) Gamma 1 band, 32–45 Hz. (E) Gamma 2, 45–67 Hz. On plots, boxes represent 25–75% quartiles, middle point median, bars denote full range. * - $p < 0.05$; ** - $p < 0.01$; *** - $p < 0.001$ between indicated groups, Kruskal-Wallis ANOVA with post-hoc median test for between-group differences.

between combined “high-frequency” (alpha, beta, gamma1, and gamma2) power and delta power. This was found to be satisfactorily normal and was modeled with ANOVA,

revealing significant group effect: $F(4, 26) = 7.1745$, $p = 0.0005$; HSD post hoc testing revealed this corresponds to an increase in the ratio of high/low activity in

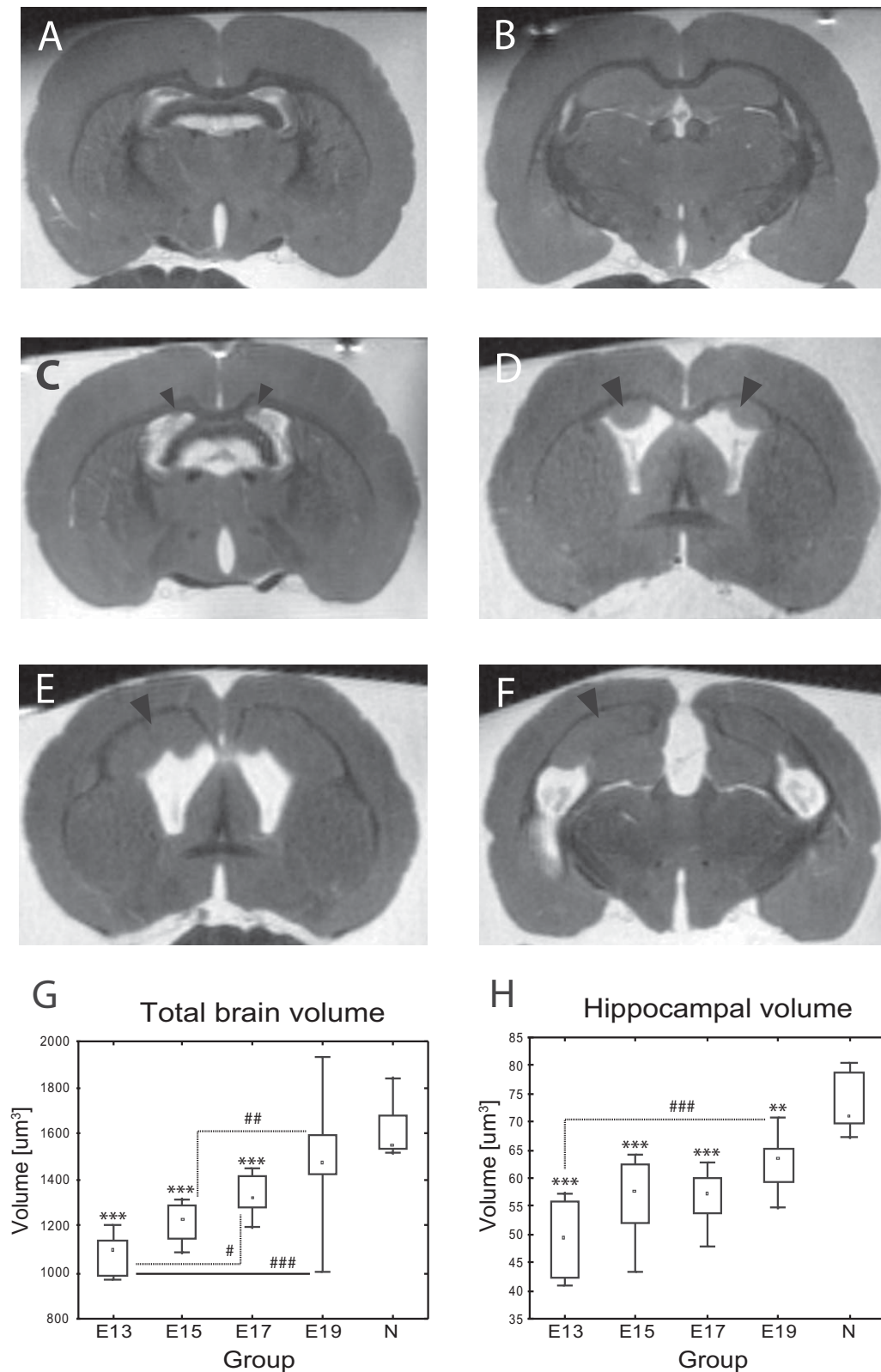


FIGURE 2. Representative MRI ex-vivo images of coronal sections through normally developed, untreated control brains (A, B) as well as dysplasia patterns observed in experimental animals. Mild changes (C) mostly include small periventricular heterotopic nodules. Moderate (D) are characterized by much larger heterotopias and visibly enlarged ventricles. Severe dysplasia (E, F) includes very large heterotopic masses, dysgenesis of the corpus callosum and significant reductions in overall brain volume. G, H – whole brain and hippocampal volumes estimated with the Cavalieri method. *** - $p < 0.001$ vs control; # - $p < 0.05$; ## - $p < 0.01$; ### - $p < 0.001$ between indicated groups, ANOVA with Tukey's HSD.

E15 (mean \pm SD: 1.684 ± 0.47) in comparison with the other groups: E13 (1.058 ± 0.31 ; $p = 0.01$), E17 (1.022 ± 0.24 ; $p = 0.009$), E19 (0.908 ± 0.24 ; $p = 0.002$), and controls (0.809 ± 0.21 ; $p = 0.002$; Fig. 1F).

MRI: QUALITATIVE OBSERVATIONS

Previously, we have described anatomical and cytoarchitectonic abnormalities in adult rats gamma-irradiated at different time points during gestation (Setkowicz et al., 2014). These anomalies, as seen in T2-weighted MRI, can be classified into three different severities: mild, with small heterotopic nodules present in the ventricles (Fig. 2C); moderate, with larger heterotopias, often found inside the white matter of corpus callosum (Fig. 2D); and severe. This final phenotype, reminiscent of lissencephaly, presents with cortical thinning, white matter dysgenesis, and very large subcortical heterotopias, in the form of marble-like structures consisting of grey matter isointense with normal cortex, but surrounded and partially penetrated by bands of white matter (Fig. 2E, F).

The time of irradiation determines the frequency and type of anatomical abnormalities, with mild nodular heterotopias present mostly in the E17 group and the most severe phenotype confined to a subset of animals from the E13 group, while E15 represents an intermediate population. Animals irradiated late (E19) are mostly free from gross anatomical malformations of this type (see Table 1 for frequency data). These differences are highly significant (Pearson's Chi-squared; $p < 0.00001$).

MRI: VOLUME ESTIMATION AND EFFECT ON EEG BAND POWER

Brain volumes, as estimated by the Cavalieri method, follow a simple relationship with the time of irradiation (ANOVA $F(4, 44) = 22.899$; $p < 0.00001$), with smallest brain volumes found in E13 (mean \pm SD: 1082 ± 89.39 ; HSD posttest $p = 0.01$ vs. E17 and 0.0001 vs. E19 and N), followed by E15 (1218 ± 86.98 ; $p = 0.001$ vs. E19 and 0.0001 vs. N), E17 (1340 ± 77.94 ; $p = 0.0009$ vs. N), E19 (1489 ± 259.93), and nonirradiated controls (1607 ± 104.34 ; Fig. 2G).

Hippocampal volume (Fig. 2H) follows a similar relationship (ANOVA $F(4, 44) = 28.273$; $p < 0.00001$), with all groups of irradiated animals—E13 (mean \pm SD: 49.17 ± 7.25 ; $p = 0.0001$), E15 (mean \pm SD: 56.27 ± 6.32 ; $p = 0.0001$), E17 (mean \pm SD: 56.53 ± 4.26 ; $p = 0.0001$), and E19 (mean \pm SD: 62.65 ± 4.93 ; $p = 0.009$)—exhibiting reduced volumes in comparison to untreated controls (72.76 ± 4.68) based on HSD posthoc testing. In addition, the group treated at the earliest time point (E13) had significantly reduced hippocampal volume when compared with the late irradiated group E19 ($p = 0.0008$).

To determine whether the presence of heterotopias could be associated with altered EEG composition, additional comparisons were made. Data from 20 animals from groups E13, E15, E17 (where heterotopias were commonly present) were pooled and assigned into two groups:

heterotopic, comprising mild, moderate and severe cases, and nonheterotopic, that is, animals without any abnormalities visible in MRI. In total, there were ten heterotopic and ten normal animals. The ratio of high to low frequency band power was then compared between these groups (by Student's t test). No effect of the presence of heterotopias was found: $t(18) = 0.069$, $p = 0.94$; means \pm SD: 1.21 ± 0.49 and 1.19 ± 0.33 in animals without heterotopias and with any visible heterotopias, respectively.

To explore the potential relationship between gross anatomy obtained with MRI and EEG composition, linear models were fitted for the effects of the experimental group, the volume of the structure of interest (i.e., hippocampal or whole brain volume) as well as their interaction. Volumes were first expressed as Z-scores and EEG composition was represented by the high/low power ratio. This way, in every model the intercept could be interpreted as the estimated ratio of high/low power in normal animals with mean volume and coefficients represent the estimated change between groups or change associated with the increase of volume by 1 SD.

Model 1: fitting the effects of group, brain volume and interaction; $F(9, 21) = 3.537$, $p = 0.008$; estimated coefficients significantly different from 0 (based on t test): intercept (estimated value: 1.026; SE: 0.49; $t = 2.104$; $p = 0.04$).

Model 2: fitting the effects of group, hippocampal volume and interaction; $F(9, 21) = 2.76$, $p = 0.03$; estimated coefficients significantly different from 0 (based on t test): none.

Model 3: fitting the group effect only; $F(4, 26) = 7.174$, $p = 0.0005$; estimated coefficients: intercept (0.809 ± 0.14 ; $t = 5.652$; $p < 0.00001$) and group E15 (0.8749 ± 0.19 ; $t = 4.555$; $p = 0.0001$) with other group coefficients E13 (0.2479 ± 0.17), E17 (0.2131 ± 0.18) and E19 (0.0985 ± 0.18) being n.s. ($p > 0.05$).

Only in the third model a significant (non-zero) coefficient for any of the experimental variables was obtained (group effect, E15). To compare the goodness of fit of these models, AIC values were calculated for each, resulting in AIC = 21.438 for Model 1, AIC = 25.841 for Model 2 and AIC = 16.983 for Model 3. Thus, the relative likelihood of Models 1 and 2 being preferable to Model 3 in terms of minimizing estimated information loss was low: 0.108 for Model 1 and 0.012 for Model 2. Thus, Model 3, containing only the group effect without any effects of volumetric variables, should be considered superior, leading to a conclusion that there is no evidence of significant effect of brain or hippocampal volume on EEG composition in these animals.

IMMUNOBLOTTING AND IMMUNOPOSITIVE AREA FRACTION

Significantly decreased levels of glutamate receptor subunit Glur4 were found in E19 (mean \pm SD: 0.152 ± 0.042) compared with E13 (0.253 ± 0.042 ; ANOVA $F(2, 25) = 4.0$

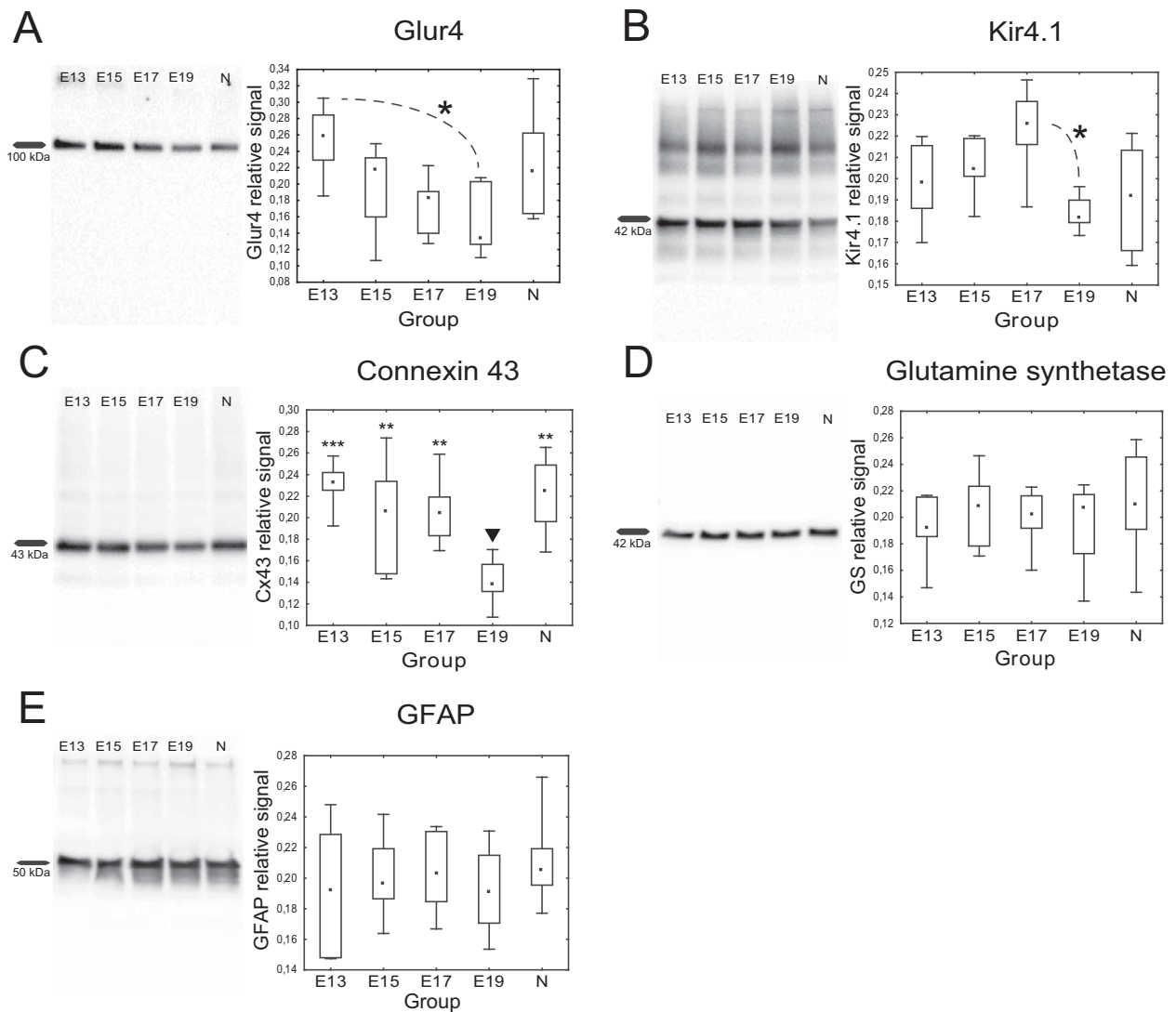


FIGURE 3. Representative blots and quantified signal normalized to overall per-lane protein load (Stain-free signal) for GFAP (A), connexin 43 (B), GS (C), Glur4 (D), and Kir4.1 (E). * - $p < 0.05$ between indicated groups, ANOVA with Tukey's HSD.

$p = 0.01$ with Tukey's HSD $p = 0.02$; Fig. 3A). Kir4.1 appeared to have (statistically nonsignificant) trend toward gradual increase from E13 to E17, but was instead sharply reduced in E19 (0.184 ± 0.008) compared with E17 (0.223 ± 0.021 ; ANOVA $F(4, 25) = 4.0258$; $p = 0.01$ with Tukey's HSD $p = 0.02$; Fig. 3B). A striking reduction in Cx43 in E19 (0.140 ± 0.022), compared with all other experimental groups (E13: 0.230 ± 0.022 $p = 0.001$; E15: 0.201 ± 0.052 $p = 0.01$ and E17: 0.206 ± 0.031 $p = 0.01$), as well as controls (0.221 ± 0.035 $p = 0.01$), was also found (ANOVA $F(2, 25) = 6.3329$, $p = 0.001$; Fig. 3C). Conversely, no significant changes were found in expression levels of GS (ANOVA $F(4, 25) = 0.3799$; $p = 0.82$; Fig. 3D) and GFAP (ANOVA $F(2, 25) = 0.3742$; $p = 0.82$; Fig. 3E).

Total hippocampal area fraction immunopositive for GFAP (Fig. 4C) was also significantly decreased (ANOVA $F(4, 61) = 3.9925$; $p = 0.006$) in E17 (0.374 ± 0.027 ; $p = 0.03$) and E19 (0.366 ± 0.040 ; $p = 0.02$) in comparison to nonirradiated controls (0.415 ± 0.029).

DISCUSSION

In the present study, we quantitatively described the patterns of prenatal irradiation-induced dysplasia in relation to their time of onset (E13–E19). This included MRI-based estimates of brain and hippocampal volume, the frequency and severity of brain heterotopias, astrocytic protein expression and immunoreactive area fraction, and finally, relative EEG power profiles of adult, freely moving rats with different patterns of

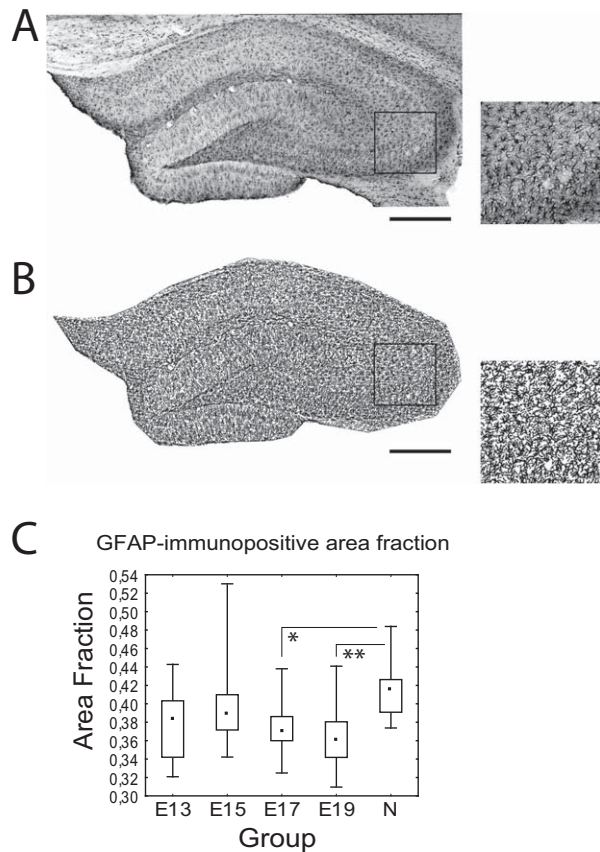


FIGURE 4. Local thresholding used for immunopositive area fraction measurements. (A) Representative panoramic image of GFAP-stained hippocampus, reconstructed from a series of images taken under a 10 \times objective. (B) The same image after thresholding. Scale bars: 100 μ m. Insets: outlined area under 4 \times zoom. (C) Immunopositive area fraction obtained from thresholded images. * - $p < 0.05$; ** - $p < 0.01$ between indicated groups, ANOVA with Tukey's HSD.

brain dysplasia. The time points explored correspond to some of the critical steps in the developmental sequence of the telencephalon: subventricular zone organization at E13, critical point for the generation of precursors giving rise to GABAergic cells at E15; peak proliferation in the hippocampus at E17; and a switch from neurogenic to gliogenic programs of gene expression in precursor cell populations at around E19 (Miller and Gauthier, 2007; Khalaf-Nazzal and Francis, 2013; Wilkinson et al., 2013).

GROSS ANATOMICAL CHANGES DIFFERENTIATE PATTERNS OF CEREBRAL DYSPLASIA

Cerebral and hippocampal volumes exhibited a simple, time dependent response: the earlier in development irradiation took place, the more dramatic effects were observed, potentially because at earlier time points any damaged progenitor cell would give rise to more daughter cells. Conversely, the underlying anatomical features, heterotopia and white

matter abnormalities, are surprisingly the most common in E17. No animals from this group were free from lentiform, periventricular heterotopic nodules. In the E13 and E15 groups, almost half the animals exhibited no discernible anomalies, although if heterotopias were present, they tended to be more severe compared with the predominantly small nodules seen in E17s. Possible explanations remain highly speculative, but could involve different modes of migration (translocation, in which the nucleus moves along a pia-directed process, which later gives way to simple locomotion, the latter being potentially more prone to disturbance), or different densities of specific precursor populations, for example, *Pax6*+*P-vim*+*Sox2*+ cells, which peak around E16 in mice (Kriegstein and Noctor, 2004; Wang et al., 2011). This window of vulnerability appears brief, as at E19, the frequency of heterotopia dropped sharply, in line with previous observations (Roper, 1998; Setkiewicz et al., 2014).

ASTROCYTES MAY PLAY A ROLE IN LATE-INDUCED CEREBRAL DYSPLASIA

The observed patterns of glial marker expression were in agreement with the idea that precursors are directed toward gliogenesis later in prenatal development, as well as our previous results, where reduced numbers of S100b-positive glia were found only in rats irradiated at E19 (Janeczko et al., 1999). A marked reduction of several astrocytic proteins: Kir4.1, connexin 43 and Glur4 was found in E19 only. These markers, initially described in the context of dysplasia in samples taken from cortical tubers in tuberous sclerosis complex patients (Sosunov et al., 2008; Talos et al., 2008), share a bidirectional relationship with epilepsy. Their ablation can directly lead to seizures, but in epileptic tissue their expression is actually often enhanced, likely as a form of adaptive plasticity aimed at responding to abnormal neuronal activity (Brand-Schieber et al., 2004; Caracciolo et al., 2011; Carlen, 2012; Sukigara et al., 2014; Ohno et al., 2015).

The relative decrease in the expression of these markers at baseline (nonepilepsy) conditions, could thus potentially result in abnormal glial function (e.g., insufficient connexin coupling) or diminished ability to respond to increased excitation. At the same time, conspicuous astrogliosis is not observed in any of our experimental animals, as there is no reduction of glutamate synthetase expression (Eid et al., 2012) and no change in total GFAP content. The lowered GFAP immunopositive area fraction in E17 and E19 would thus likely correspond not to decreased *total* expression of GFAP, but likely to altered (more sparse) alignment of glial processes. The larger GFAP + processes form a backbone for the smaller processes responsible for astrocyte-neuron interactions (Bushong et al., 2002; Hirrlinger et al., 2004).

BASELINE PATTERNS OF BRAIN ACTIVITY ARE DIFFERENTIALLY AFFECTED AT DISTINCT TIME POINTS

EEG composition in dysplastic animals varied significantly between time points: in E13s, it was unchanged in comparison to controls, while in the groups E15 to E19, a time-dependent opposite regulation of high- and low-frequency activity was apparent. E15 was the most affected, with sharp decrease in delta accompanied by increased alpha/beta and gamma components, while in E17 through E19 this effect is reversed, with E19 being again close to normal. The “theta” frequencies (corresponding to 6–10 Hz) were unaffected and seemed to be a “breakpoint” between oppositely regulated low- and high-frequency components (Scheeringa et al., 2011). This underscores the apparent lack of spike-wave discharges or other spontaneous epileptiform activity in our animals, as these events would have probably contributed to this band (Kandel and Buzsáki, 1997). Some degree of interictal spiking was previously reported in E17s by investigators from S.N. Roper’s group (Kondo et al., 2001; Kellinghaus et al., 2004). The apparent difference could be explained by different rats used, Wistar versus SD (Shaw, 2007; Pearce et al., 2014), or longer resting period between implantation and recording, as the previous studies have been performed 48h after surgery.

LARGE-SCALE ANATOMICAL CHANGES DO NOT CORRELATE TO EEG PATTERNS

The relationship between brain and hippocampal volumes obtained from MRI and EEG composition was modeled to test whether large-scale anatomy could potentially contribute to between-group differences in EEG power. There was, however, no evidence of significant effects of reduced brain as well as hippocampal volume on EEG composition. We then looked at heterotopia as a possible correlate of EEG activity. However, here, too, no relationship was found between EEG power and the anatomical phenotype. This is clear when considering the fact that E13 and E15, while exhibiting similar patterns of heterotopia, differed greatly in EEG composition, which was strongly altered in E15, but not so in E13. While subcortical heterotopia and other focal lesions can potentially be recruited into cortical networks in humans (Duchowny, 2009), it is possible that this was not the case here, or otherwise the epidural EEG recordings were unable to pick up or differentiate such activity.

If neither the degree of neuronal heterotopia nor the loss of tissue volume are good predictors of EEG spectral composition, more subtle, cellular changes could be hypothesized to play a more prominent role. In particular, reduced density and decreased functional efficacy of GABAergic interneurons has been previously reported in humans and in irradiation-induced dysplastic rat cortex (Roper et al., 1999; Akakin et al., 2013). At first glance, this is hard to reconcile with current results, as loss of interneurons should correspond to decrease, rather than the observed increase, in the gamma band. Fast-spiking

interneurons are crucial for driving this type of EEG activity (Meletis et al., 2009).

There are, however, some considerations that could shed more light on the matter. The interneuronal populations contributing to gamma activity are predominantly located in outer layers of the cortex, specifically layers II–III (Roopun et al., 2006; Scheeringa et al., 2016). In FCD usually the deeper layers are more affected, with reduction in interneuron density mostly seen in layer IV, but not layers II–III, which might indeed have normal, or even increased, densities of interneurons (Kuchukhidze et al., 2015; Nakagawa et al., 2017). Differences between FCD type I and type II has also been reported, with considerable interneuron loss in type II, but not type I, in fact, GABA current densities and effective concentration have been shown to be unchanged, or even elevated in type I dysplastic cortex (André et al., 2010). This could be caused by a displacement of neurons between layers, as evidenced by shifted expression of typically layer-specific markers in dysplastic cortex (Rossini et al., 2011).

Caution is needed when interpreting these findings, especially when attempting to compare between results from human patients with FCD type I/II and animal models. It is, however, worth noting that, while our previous investigation of cortical sections of rats from the E13 to E19 groups with autoradiography found evidence of some redistribution and general reduction in neuronal density during development (Setkowicz et al., 2014), these were not accompanied by significantly decreased densities of cortical parvalbumin- or calretinin-positive neurons. Subsequent investigation of interneuron immunostaining in adult rats yielded some preliminary results in the form of increased density of parvalbumin interneurons in layer II, with concomitant decrease in the deeper layers (unpublished observation). This is currently under investigation and of potential interest, if confirmed.

There are also other mechanisms that could contribute to EEG composition; notably, astrocytes play a role in generating gamma band EEG activity, inhibition of glial metabolism, or exocytosis has been shown to inhibit activity in the 20 to 100 Hz range (Willoughby et al., 2005; Lee et al., 2014) and be potentially seizurogenic. Because changes in astrocytes seem to be confined mostly to the late-irradiated rat brains, notably E19, it is possible that glial hypofunction could contribute to the shift from predominantly high-frequency to predominantly low-frequency EEG activity observed from E15 to E19.

CONCLUSIONS

In summary, there are significant differences between patterns of dysplasia evoked at different time points from E13 to E19 in terms of baseline EEG composition. These differences are likely not related to gross anatomical changes, such as volume reduction or heterotopia, but are rather mediated by more specific alterations in functional

properties or spatial arrangement of cell populations, with (predominantly parvalbumin-expressing) interneurons and astrocytes as potential targets with counteractive effects. A more complete understanding of these mechanisms could be useful not only due to the fact that different patterns of dysplasia correspond to differentially altered susceptibility to seizures (Setkovicz et al., 2005, 2014), but also because regulation of gamma activity itself has been implicated both in humans and in animal models of epilepsy (Pan et al., 2009; Tchekalarova et al., 2016).

We are currently investigating these mechanisms further, by analyzing gene transcriptional profiles of the E13 to E19 groups (submitted), as well as assessing seizure reactivity and its cellular correlates. In the future, the time-specific design could prove a useful extension of the currently used model (based on E17). The different time points have unique potential benefits: E15 exhibits highly altered baseline EEG activity, E17 is highly stable in regard to brain structure (i.e., heterotopia), while E19 could provide the opportunity to study astrocyte-related mechanisms.

ACKNOWLEDGEMENTS

K.J. was funded by a Polish National Science Centre grant.

REFERENCES

- Akakin D, Martinez-Diaz H, Chen H-X, Roper SN. 2013. Reduced densities of parvalbumin- and somatostatin-expressing interneurons in experimental cortical dysplasia and heterotopia in early postnatal development. *Epilepsy Res* 104:226–233.
- André VM, Cepeda C, Vinters HV, et al. 2010. Interneurons, GABA currents, and subunit composition of the GABA A receptor in type I and type II cortical dysplasia. *Epilepsia* 51(Suppl 3):166–170.
- Barkovich AJ, Guerrini R, Kuzniecky RI, et al. 2012. A developmental and genetic classification for malformations of cortical development: update 2012. *Brain* 135(Pt 5):1348–1369.
- Blümcke I, Thom M, Aronica E, et al. 2011. The clinicopathologic spectrum of focal cortical dysplasias: a consensus classification proposed by an ad hoc Task Force of the ILAE Diagnostic Methods Commission. *Epilepsia* 52:158–174.
- Brand-Schieber E, Lowery SL, Werner P. 2004. Select ionotropic glutamate AMPA/kainate receptors are expressed at the astrocyte-vessel interface. *Brain Res* 1007:178–182.
- Bushong EA, Martone ME, Ellisman MH. 2004. Maturation of astrocyte morphology and the establishment of astrocyte domains during postnatal hippocampal development. *Int J Dev Neurosci* 22:73–86.
- Bushong EA, Martone ME, Jones YZ, Ellisman MH. 2002. Proto-plasmic astrocytes in CA1 stratum radiatum occupy separate anatomical domains. *J Neurosci* 22:183–192.
- Caracciolo L, Barbon A, Palumbo S, et al. 2011. Altered mRNA editing and expression of ionotropic glutamate receptors after Kainic Acid exposure in cyclooxygenase-2 deficient mice. *PLoS One* 6:e19398.
- Carlen PL. 2012. Curious and contradictory roles of glial connexins and pannexins in epilepsy. *Brain Res* 1487:54–60.
- Chen HX, Xiang H, Roper SN. 2007. Impaired developmental switch of short-term plasticity in pyramidal cells of dysplastic cortex. *Epilepsia* 48:141–148.
- Degasperi A, Birtwistle MR, Volinsky N, et al. 2014. Evaluating strategies to normalise biological replicates of western blot data. *PLoS One* 9:e87293.
- Duchowny M. 2009. Clinical, functional, and neurophysiologic assessment of dysplastic cortical networks: Implications for cortical functioning and surgical management. *Epilepsia* 50(Suppl 9): 19–27.
- Eid T, Behar K, Dhaher R, et al. 2012. Roles of glutamine synthetase inhibition in epilepsy. *Neurochem Res* 37:2339–2350.
- Gulati S, Yoganathan S, Chakrabarty B. 2014. Epilepsy, cognition and behavior. *Indian J Pediatr* 81:1056–1062.
- Harvey S, Cross JH, Shinnar S, et al. 2008. Defining the spectrum of international practice in pediatric epilepsy surgery patients. *Epilepsia* 49:146–155.
- Hiremath GK, Tilelli CQ, Xu Y, et al. 2009. Gene expression changes in an animal model of in utero irradiation-induced cortical dysplasia. *Epileptic Disord* 11:232–243.
- Hirrlinger J, Hülsmann S, Kirchhoff F. 2004. Astroglial processes show spontaneous motility at active synaptic terminals in situ. *Eur J Neurosci* 20:2235–2239.
- Janeczko K, Setkovicz Z, Fraczek M, Kochowska J. 1999. Effects of prenatal gamma-irradiation on postnatal astrogliogenesis in the hippocampal formation of rat. *Brain Res* 816:628–632.
- Kandel A, Buzsáki G. 1997. Cellular-synaptic generation of sleep spindles, spike-and-wave discharges, and evoked thalamocortical responses in the neocortex of the rat. *J Neurosci* 17: 6783–6797.
- Kellinghaus C, Kunieda T, Ying Z, et al. 2004. Severity of histopathologic abnormalities and in vivo epileptogenicity in the in utero radiation model of rats is dose dependent. *Epilepsia* 45: 583–591.
- Khalaf-Nazzal R, Francis F. 2013. Hippocampal development – old and new findings. *Neuroscience* 248:225–242.
- Kielbinski M, Gziel K, Soltys Z. 2016. Review: Roles for astrocytes in epilepsy: insights from malformations of cortical development. *Neuropathol Appl Neurobiol* 42:593–606.
- Kondo S, Najm I, Kunieda T, et al. 2001. Electroencephalographic characterization of an adult rat model of radiation-induced cortical dysplasia. *Epilepsia* 42:1221–1227.

- Kriegstein AR, Noctor SC. 2004. Patterns of neuronal migration in the embryonic cortex. *Trends Neurosci* 27:392–399.
- Krsek P, Jahodova A, Maton B, et al. 2010. Low-grade focal cortical dysplasia is associated with prenatal and perinatal brain injury. *Epilepsia* 51:2440–2448.
- Kuchukhidze G, Wieselthaler-Hölzl A, Drexel M, et al. 2015. Calcium-binding proteins in focal cortical dysplasia. *Epilepsia* 56:1207–1216.
- Lee HS, Ghetti A, Pinto-Duarte A, et al. 2014. Astrocytes contribute to gamma oscillations and recognition memory. *Proc Natl Acad Sci U S A* 111:E3343–E3352.
- Lerner JT, Salamon N, Hauptman JS, et al. 2009. Assessment and surgical outcomes for mild type I and severe type II cortical dysplasia: a critical review and the UCLA experience. *Epilepsia* 50:1310–1335.
- Luhmann HJ. 2015. Models of cortical malformation-chemical and physical. *J Neurosci Methods* 260:62–72.
- Marín-Padilla M, Parisi JE, Armstrong DL, et al. 2002. Shaken infant syndrome: development neuropathology, progressive cortical dysplasia, and epilepsy. *Acta Neuropathol* 103:321–332.
- Meletis K, Knoblich U, Zhang F, et al. 2009. Driving fast-spiking cells induces gamma rhythm and controls sensory responses. *Nature* 459:663–668.
- Miller FD, Gauthier AS. 2007. Timing is everything: making neurons versus glia in the developing cortex. *Neuron* 54:357–369.
- Nakagawa JM, Donkels C, Fauser S, et al. 2017. Characterization of focal cortical dysplasia with balloon cells by layer-specific markers: evidence for differential vulnerability of interneurons. *Epilepsia* 58:635–645.
- Ochoa JG, Hentgarden D, Paulzak A, et al. 2017. Subtle pathological changes in neocortical temporal lobe epilepsy. *Epilepsy Behavior* 71:17–22.
- Ohno Y, Tokudome K, Kunisawa N, et al. 2015. Role of astroglial Kir4.1 channels in the pathogenesis and treatment of epilepsy. *Ther Targets Neurol Dis* 1–10.
- Pan JW, Zaveri HP, Spencer DD, et al. 2009. Intracranial EEG power and metabolism in human epilepsy. *Epilepsy Res* 87:18–24.
- Paxinos G, Watson C. 1998. The rat brain in stereotaxic coordinates. New York: Academic Press. pp 1–474.
- Pearce PS, Friedman D, LaFrancois JJ, et al. 2014. Spike-wave discharges in adult Sprague-Dawley rats and their implications for animal models of temporal lobe epilepsy. *Epilepsy Behavior* 32:121–131.
- Pitkänen A, Löscher W, Vezzani A, et al. 2016. Advances in the development of biomarkers for epilepsy. *Lancet Neurol* 15:843–856.
- Roberts N, Puddephat MJ, McNulty V. 2000. The benefit of stereology for quantitative radiology. *Br J Radiol* 73:679–697.
- Roopun AK, Middleton SJ, Cunningham MO, et al. 2006. A beta2-frequency (20–30 Hz) oscillation in nonsynaptic networks of somatosensory cortex. *Proc Natl Acad Sci U S A* 103:15646–15650.
- Roper SN. 1998. In utero irradiation of rats as a model of human cerebrocortical dysgenesis: a review. *Epilepsy Res* 32:63–74.
- Roper SN, Eisenschenk S, King MA. 1999. Reduced density of parvalbumin- and calbindin D28-immunoreactive neurons in experimental cortical dysplasia. *Epilepsy Res* 37:63–71.
- Roper SN, Gilmore RL, Houser CR. 1995. Experimentally induced disorders of neuronal migration produce an increased propensity for electrographic seizures in rats. *Epilepsy Res* 21:205–219.
- Rossini L, Moroni RF, Tassi L, et al. 2011. Altered layer-specific gene expression in cortical samples from patients with temporal lobe epilepsy. *Epilepsia* 52:1928–1937.
- Scheeringa R, Fries P, Petersson KM, et al. 2011. Neuronal dynamics underlying high- and low-frequency EEG oscillations contribute independently to the human BOLD signal. *Neuron* 69:572–583.
- Scheeringa R, Koopmans PJ, van Mourik T, et al. 2016. The relationship between oscillatory EEG activity and the laminar-specific BOLD signal. *Proc Natl Acad Sci U S A* 113:6761–6766.
- Setkowicz Z, Gzielo-Jurek K, Uram Ł, et al. 2014. Brain dysplasia evoked by gamma irradiation at different stages of prenatal development leads to different tonic and clonic seizure reactivity. *Epilepsy Res* 108:66–80.
- Setkowicz Z, Janicka D, Kowalczyk A, et al. 2005. Congenital brain dysplasias of different genesis can differently affect susceptibility to pilocarpine- or kainic acid-induced seizures in the rat. *Epilepsy Res* 67:123–131.
- Setkowicz Z, Klak K, Janeczko K. 2003. Long-term changes in postnatal susceptibility to pilocarpine-induced seizures in rats exposed to gamma radiation at different stages of prenatal development. *Epilepsia* 44:1267–1273.
- Shaw F-Z. 2007. 7–12 Hz high-voltage rhythmic spike discharges in rats evaluated by antiepileptic drugs and flicker stimulation. *J Neurophysiol* 97:238–247.
- Sosunov AA, Wu X, Weiner HL, et al. 2008. Tuberous sclerosis: a primary pathology of astrocytes? *Epilepsia* 49(Suppl 2):53–62.
- Sukigara S, Dai H, Nabatame S, et al. 2014. Expression of astrocyte-related receptors in cortical dysplasia with intractable epilepsy. *J Neuropathol Exp Neurol* 73:798–806.
- Talos DM, Kwiatkowski DJ, Cordero K, et al. 2008. Cell-specific alterations of glutamate receptor expression in tuberous sclerosis complex cortical tubers. *Ann Neurol* 63:454–465.
- Tchekalarova J, Kortenska L, Marinov P, Boyanov K. 2016. Comparative power spectrum analysis of EEG activity in spontaneously hypertensive and Wistar rats in kainate model of temporal model of epilepsy. *Brain Res Bull* 124:62–75.

-
- Wang X, Tsai J-W, LaMonica B, Kriegstein AR. 2011. A new subtype of progenitor cell in the mouse embryonic neocortex. *Nat Neurosci* 14:555–561.
- Widdess-Walsh P, Kellinghaus C, Jeha L, et al. 2005. Electro-clinical and imaging characteristics of focal cortical dysplasia: correlation with pathological subtypes. *Epilepsy Res* 67:25–33.
- Wilkinson G, Dennis D, Schuurmans C. 2013. Proneural genes in neocortical development. *Neuroscience* 253:256–273.
- Willoughby JO, Mackenzie L, Pope KJ, et al. 2005. Localised astroglial dysfunction disrupts high-frequency EEG rhythms. *J Neural Transm* 112:205–213.
- Wong M, Roper SN. 2016. Genetic animal models of malformations of cortical development and epilepsy. *J Neurosci Methods* 260:73–82.
- Zhou F-W, Rani A, Martinez-Diaz H, et al. 2011. Altered behavior in experimental cortical dysplasia. *Epilepsia* 52:2293–2303.
- Zhou F-W, Roper SN. 2011. Altered firing rates and patterns in interneurons in experimental cortical dysplasia. *Cereb Cortex* 21:1645–1658.
- Zhou F-W, Roper SN. 2012. Impaired hippocampal memory function and synaptic plasticity in experimental cortical dysplasia. *Epilepsia* 53:850–859.
- Zhou F-W, Roper SN. 2014. Reduced chemical and electrical connections of fast-spiking interneurons in experimental cortical dysplasia. *J Neurophysiol* 112:1277–1290.
- Zhu WJ, Roper SN. 2000. Reduced inhibition in an animal model of cortical dysplasia. *J Neurosci* 20:8925–8931.